

Firebrand transport from a novel firebrand generator: numerical simulation of laboratory experiments

R. Wadhvani, D. Sutherland, A. Ooi and K. Moinuddin

International Journal of Wildland Fire 31, 634–648

The authors wish to advise of errors in the above paper.

- (1) On page H the line ‘... particle densities respectively of cubi-form particles = 428 kg m³⁻³. In the experiments, ...’ should read ‘... particle densities respectively of cubi-form particles = 428 kg m⁻³ and 48 kg m⁻³. In the experiments, ...’
- (2) The incorrect supplementary material file was published along with the paper. The correct file has now been uploaded to show the correct title and to include missing sub-captions.

Firebrand transport from a novel firebrand generator: numerical simulation of laboratory experiments

R. Wadhvani^{A,B}, D. Sutherland^{B,C}, A. Ooi^{B,D} and K. Moinuddin^{A,B,*}

For full list of author affiliations and declarations see end of paper

***Correspondence to:**

K. Moinuddin
Centre for Environmental Safety and Risk
Engineering, Victoria University,
Melbourne, Vic. 3030, Australia
Email: khalid.moinuddin@vu.edu.au

ABSTRACT

Firebrands (often called embers) increase the propagation rate of wildfires and often cause the ignition and destruction of houses. Predicting the motion of firebrands and the ignition of new fires is therefore of significant interest to fire authorities. Numerical models have the potential to accurately predict firebrand transport. The present study focuses on conducting a set of benchmark experiments using a novel firebrand generator, a device that produces controlled and repeatable sets of firebrands, and validating a numerical model for firebrand transport against this set of experiments. The validation is conducted for the transport of non-burning and burning cubiform firebrand particles at two flow speeds. Four generic drag sub-models used to estimate drag coefficients that are suited for a wide variety of firebrand shapes are verified for their applicability to firebrand transport modelling. The four sub-models are found to be good in various degrees at predicting the transport of firebrand particles.

Keywords: contour, contour peak location, drag models, embers, Fire Dynamics Simulator, firebrand generator, Lagrangian particles, lateral spread, short-range firebrands.

Introduction

Firebrands are a primary cause of the increased rate of fire spread inside a forest canopy and can cause damage to structures located close to a forest. The whole process encompassing the transport of firebrands and their propensity to ignite surface fuels or structures is called spotting. Short-range (where the firebrands travel up to 750 m) spotting is principally observed inside the forest canopy where the firebrands travel mainly owing to shear stress of wind, with little to no lofting provided by the buoyant force of the sub-canopy fire (Cruz *et al.* 2015). Massive short-range spotting can increase the observed rate of fire spread up to three times compared with the rate of fire spread when firebrands are not present; this effect was observed in the 1962 Daylesford fire, Victoria, Australia (McArthur 1967). Thus, it is imperative to account for short-range spotting in fire spread simulations explicitly, especially for vegetation types such as eucalyptus and pine forests, which produce significant numbers of firebrands. It is extremely challenging to conduct field-scale measurements owing to safety hazards to personnel and equipment during the experiment, as well as the associated expense and the limits of experimental parameters that are achievable. Some field-scale research studies with actual vegetation (Gould *et al.* 2008; El Houssami *et al.* 2016; Filkov *et al.* 2017; Thomas *et al.* 2017; Storey *et al.* 2020) have quantified short-range spotting distances, and firebrand material, sizes and mass, from a forest with limited parameters affecting the firebrand transport.

Numerical approaches to quantify the behaviour of short-range spotting offer more convenience to develop a short-range firebrand model that can be incorporated in an operational fire model. Tarifa and co-workers (Tarifa *et al.* 1965; Tarifa 1967) were the first who attempted to develop a correlation between different types of firebrand and their maximum spotting distance. However, their work focused on firebrands that were lofted by the plume, representing long-range spotting firebrands, to develop a spotting model. Similarly, Albin (1979) also developed a spotting model for long-range firebrands that has been widely used in various operational fire models. Tse and Fernandez-Pello (1998)

Received: 18 June 2021
Accepted: 13 April 2022
Published: 13 May 2022

Cite this:

Wadhvani R *et al.* (2022)
International Journal of Wildland Fire
31(6), 634–648. doi:10.1071/WF21088

© 2022 The Author(s) (or their employer(s)). Published by CSIRO Publishing on behalf of IAWF.

carried out numerical modelling for spherical metallic firebrand particles (representing sparks from power cables) and wooden firebrand particles coming from a tree. The work focused on understanding the trajectory of firebrands ejected at a certain height from the ground into the surface layer flow (30–50 m from the ground) and their ignition potential to cause spotting. However, they did not develop any correlation that could be used in an operational fire model representing various type of firebrands in a wildfire. [Sardoy *et al.* \(2008\)](#) conducted the first numerical study with a correlation between short-range firebrands and fire size. [Sardoy *et al.*](#) simulated firebrand transport by conducting three-dimensional (3D) physics-based modelling for the transport of different disc-shaped firebrands from the plume generated in a line fire source. They developed a correlation between firebrand parameters and ambient parameters like fire intensity and wind speed. Their model revealed a bimodal distribution of the firebrands on the ground downstream when both pyrolysis and char oxidation were present in the firebrand. Some of the firebrands, mostly in a flaming state, landed a short distance from the source fire and other firebrands, in a charred state, landed a long distance from the source fire. However, the quantification of error and uncertainty associated with their model was not computed nor was the model compared with any field-scale experiments or real wildfire incidents.

Simulations results from physics-based fire models must be carefully validated against experiments with burning firebrands. The validation of a model is challenging at field-scale because of difficulties in controlling experimental parameters that affect the repeatability of the experiment. These challenges can be exacerbated by the settlement of communities close to forests, which restricts the locations of the experiments. An alternative is to conduct the validation work at a laboratory scale and then scale up the simulations and compare them with documented wildfire incidents ([Linteris *et al.* 2004](#)).

The Firebrand Dragon constructed by the National Institute of Standards and Technology (NIST) in the USA ([Manzello *et al.* 2008](#)) is one such apparatus, and can produce artificial firebrand showers in a meticulous and repeatable manner. The NIST Firebrand Dragon has been mainly used to study the impact of firebrands on structures ([Manzello and Suzuki 2013, 2014](#); [Suzuki *et al.* 2016](#)) and the ignition of forest surface fuel ([Manzello *et al.* 2006](#)). [Kortas *et al.* \(2009\)](#) validated a particle transport model for the transport of cylindrical and disc-shaped firebrands used in the NIST Firebrand Dragon. They compared mass loss and longitudinal travel distance distribution, although they ignored collisions between the firebrand particles and the wall of the Firebrand Dragon. The NIST Firebrand Dragon has a bend at the mouth, which produces a Dean's vortex near the mouth ([Wadhvani *et al.* 2017b](#)). The Lagrangian assumption for particle modelling would not be valid to use with the NIST Firebrand Dragon owing to particle interactions and

modification of flow due to the large number of particles. It is to be noted that [Kortas *et al.* \(2009\)](#) assumed a Weibull distribution of firebrands leaving the Dragon mouth as the initial condition to match with the experiments. [Wadhvani *et al.* \(2017b\)](#) constructed a firebrand generator prototype that produces a uniform shower of firebrands to validate the Lagrangian particle model of the Fire Dynamics Simulator (FDS). FDS is a physics-based fire model that has been extensively used in fire sciences for building and wildland fires ([McGrattan *et al.* 2015a](#)). However, their work was limited to testing the performance of the inbuilt drag model of FDS for non-burning particles.

The present work is built on that of [Wadhvani *et al.* \(2017b\)](#) to study burning firebrands by constructing an entirely new firebrand generator. Compared with [Wadhvani *et al.* \(2017b\)](#), there are two main improvements to the generator. The generator described here is constructed of stainless steel to produce uniform burning firebrands, which was not possible in the prototype generator constructed of polyvinyl chloride (PVC). The new generator also allows control of the flow Reynolds numbers, accommodates different sizes of firebrand, and can produce a wide range of combustible firebrands. The experimental data are valuable as a benchmark set for any model validation. Realistic firebrands are found to be considerably different in size, shape and stages of combustion, as observed in field studies ([Gould *et al.* 2008](#); [El Houssami *et al.* 2016](#); [Filkov *et al.* 2017](#); [Thomas *et al.* 2017](#); [Storey *et al.* 2020](#)). Although there has been some work on cylindrical firebrands ([Tohidi and Kaye 2017](#)), firebrand particles are often assumed purely spherical ([Thurston *et al.* 2017](#); [Thomas *et al.* 2020](#)). This assumption likely leads to significant inaccuracies in predicted landing distributions. A simplifying assumption for long-range firebrands is a constant terminal velocity, which has been shown to overpredict the landing density of firebrands ([Thomas *et al.* 2020](#)). Therefore, accounting for the shape of the firebrand is critical to improved predictions of firebrand distribution. It is also necessary to quantify differences between predicted and actual firebrand distributions to assess upper and lower limits of error.

Thus, the purpose of the computational study is twofold: (a) quantifying the assessment for a set of alternative drag models suited to represent generic shapes of firebrands using the firebrand generator; and (b) validating the firebrand transport model within a physics-based model (FDS) for burning firebrands. The validated model can then be applied to study the transport of short-range firebrands, such as firebrand transport inside a forest canopy ([Wadhvani *et al.* 2019](#)).

Experimental methodology and design of firebrand generator

The design of the firebrand generator is based on the prototype detailed in [Wadhvani *et al.* \(2017b\)](#). The critical

modifications to the base design are: (i) the addition of a firebrand heater to ignite firebrands (Fig. 1a–c), and (ii) the insertion of a honeycomb-type flow straightener (Fig. 1d) to minimise the length required to develop a uniform flow at

the mouth of the generator. The combined length of the two concentric stainless steel pipes is 3.9 m, which consists of two pipes of nominal inner diameters 50 and 200 mm and of lengths 2.3 and 3.1 m, respectively. The generator is

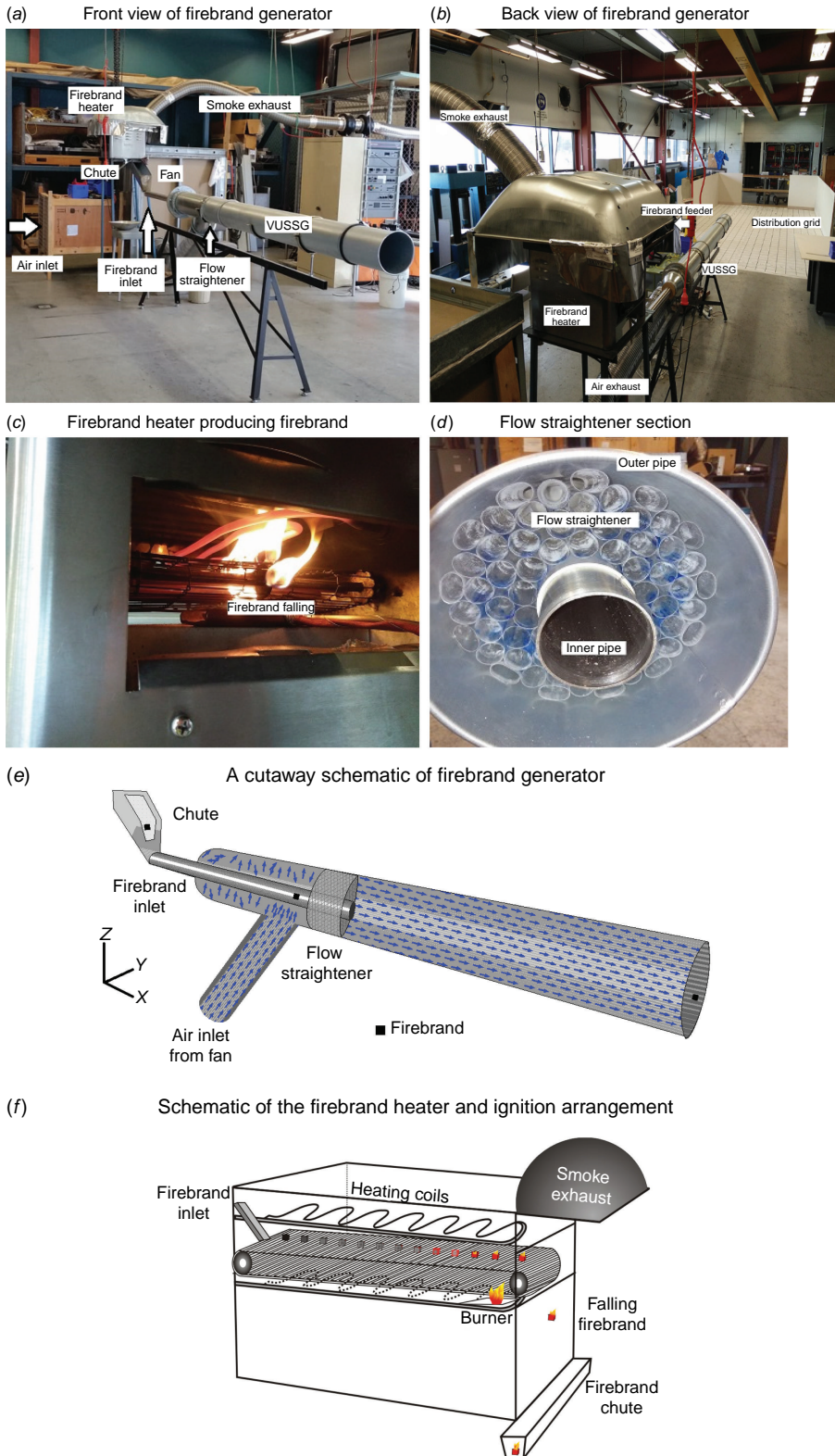


Fig. 1. Different sections of the firebrand generator highlighting its working principles and hidden features (VUSSG, Victoria University stainless steel generator).

constructed to produce varied sizes and shapes of firebrand with different degrees of combustion and at different flow speeds; however, for the current study, only burning and non-burning cubiform firebrand particles and two Reynolds numbers of the flow are studied as a proof of concept.

Fig. 1 shows the different sections of the concentric pipe firebrand generator (known as the Victoria University Stainless Steel Generator or VUSSG). Fig. 1a, b shows the front and back view of the firebrand generator highlighting the main components of the equipment. Fig. 1e provides a cutaway schematic of the firebrand generator clarifying its working principles. Air is drawn into the equipment through the ‘air inlet’ (shown in Fig. 1a) using a centrifugal fan (hidden inside the cabinet denoted ‘fan’). The air then reaches the annular region of the concentric pipes (shown in Fig. 1e) and passes through a honeycomb flow straightener. The flow provides the required acceleration to the firebrand particles coming through the inner pipe. The three-phase induction motor centrifugal fan of 7.457 kW runs at 2860 rpm in the hidden cabinet, providing air to the firebrand generator. The motor controller is used to control the speed of the fan, and thus, provides a control of flow Reynolds number. The firebrands are fed to the ‘firebrand heater’ conveyor belt (sketched in Fig. 1f), which provides them sufficient time to ignite and maintain a flaming combustion state (Fig. 1c) before they fall into the ‘firebrand inlet’ pipe via a chute (Fig. 1a, e). The firebrand heater consists of a conveyor belt and two (top and bottom) radiant heating elements that are designed to give firebrand feed rates 0.055–0.165 firebrands s^{-1} . By adjusting the conveyor belt speed, it is possible to achieve 40–75% combusted cubiform firebrand particles when both heating elements are turned on. The low firebrand feed rate is to ensure there is effectively only one-way coupling between the fluid and the particle, an essential feature of a Lagrangian model. That is, while the fluid exerts forces on the particle, the particle has a negligible effect on the flow. In a particle-laden flow, the presence of many particles can induce turbulence and particle–particle interactions can occur (Lain and Garcia 2006). These phenomena are not included in the Lagrangian particle model. In a real, ember-laden flow, we expect the ember density to be sufficiently low that a Lagrangian model is sufficient (Thurston *et al.* 2017; Thomas *et al.* 2020). A higher ember feed rate is possible but is beyond the current scope of research. The average initial mass of *Pinus radiata*-based cubiform firebrand particles used in this study was 0.83 g and the average length was 12.45 mm, identical to the particles used by Wadhvani *et al.* (2017b). During non-burning firebrand experiments, the heating elements and pilot flame are turned off. During the burning firebrand experiments, the conveyer belt runs at 0.165 firebrands s^{-1} , corresponding to 40% combusted cubiform firebrands. The firebrand heater provides a net radiative heat flux (measured using a handheld radiometer) of 25 kW m^{-2} , with the firebrands fed to the conveyor belt

of the firebrand heater at an ambient temperature of 30°C . Inside the firebrand heater, a firebrand particle heats for $45(\pm 2) \text{ s}$, exposed to net radiative heat flux of 25 kW m^{-2} and then converts to flaming combustion for $24(\pm 2) \text{ s}$ through auto-ignition or piloted ignition by a small flame while continuously receiving radiant heat flux before the firebrand falls into the chute to the firebrand inlet location.

The firebrand temperature after it leaves the heater but before it is injected into the inner pipe at the firebrand inlet location (Fig. 1a, e) of the generator was measured manually and quickly using a non-contact infrared thermometer and thermocouple to cross-verify the experimental measurements. Thirty firebrands (i.e. 12% of firebrands used in each experimental run) were paused between the heater and inlet and measured using a non-contact infrared thermometer (with emissivity of 0.97) and using a manual contact thermocouple. The measured average temperature with the infrared thermometer was 300°C and the thermocouple was 320°C , so the average temperature of the firebrand particle is taken as $310(\pm 50)^\circ\text{C}$. The average mass of firebrand particles before injection at the firebrand inlet is reduced by 57.4%, the average volume by 27.1% and the average density by 20.7% respective to their initial ambient measurement. The effective heat of combustion of the firebrand particle is 16.21 MJ kg^{-1} , the heat of reaction is $522.39 \text{ kJ kg}^{-1}$ and soot yield is $0.00192 \text{ kg kg}^{-1}$ (the measurement techniques for these quantities are detailed in Wadhvani (2019)).

The firebrand generator is utilised to generate a series of firebrands (after flow has been established to steady-state conditions) that land on the ‘distribution grid’ ($20 \times 20 \text{ cm}$) (Fig. 1b); the firebrands may then bounce and land again. Only the first-impact locations where a firebrand initially lands are measured using two high-speed cameras. The video footage is post-processed using MATLAB to extract the firebrand impact location (Wadhvani 2019). The video footage is first processed to exaggerate contrast between the particle, the marked grid lines in the landing area and the white background. The frames are then displayed and manually inspected to record the impact location. In each experimental run, 250 firebrands are used and collected, and the experimental runs are conducted until the convergence criteria (Eqns 1 and 2) are met. Experiments were run at least eight times to satisfy the criteria and the resulting cumulative distribution of overall experimental runs are considered the experimental distribution of cubiform firebrands.

$$P_i(x, y) = \frac{1}{i} \sum_{j=1}^i \frac{f_j(x, y)}{\int_{y_l}^{y_u} \int_{x_l}^{x_u} f_j(x, y) dx dy} \quad (1)$$

where i is the number of experiments, $f_j(x, y)$ is the distribution of particles for an experiment j ; x_l , y_l , x_u , y_u are the lower and upper coordinates of the distribution grid x , y . Eqn 1 takes the observed distributions from experiment j , and normalises the distribution so the integral is one (and

thus the summand is a probability density function) before averaging the distribution over i experiments. The distribution is deemed converged (Eqn 2) when the successive variation in each distribution grid is found to be less than 5%. This level of statistical convergence is found to be sufficient; a higher convergence criterion could be considered but would significantly increase the number of experimental runs (including data processing) required to achieve a high convergence level at each grid point. The convergence criteria is defined as

$$\max\{P_{i+1}(x, y) - P_i(x, y)\} < 0.05. \quad (2)$$

The Lagrangian particle model validation required the measurement of the flow velocity and particle velocity. The flow velocity was measured with a pitot tube. The particle velocity was measured using two orthogonal high-speed cameras. The measurement methodology and uncertainty associated with the measurements are discussed in Wadhvani et al. (2017b). The experiments were carried out at the higher end of the flow Reynolds numbers (Re) observed in real wildfires during short-range spotting (Gould et al. 2008; Thomas et al. 2017); two flow speeds, representative of fire conditions, are considered in this study, denoted the Re-1 case (Re no. 3×10^5) and Re-2 case (Re no. 3.4×10^5). The video footage of particle tracking at the mouth was post-processed in MATLAB to measure the distance a particle travels between individual image frames to compute particle component velocities. The average values of particle velocity for all cases are listed in Table 1. Note that u is the streamwise velocity along the axis of the tube, w is the vertical velocity of the particle, which is positive in the upwards direction measured from the centre of the tube, v is the spanwise velocity of the particle mutually orthogonal to u and w ; the positive direction follows from the standard right-hand rule. The v and w particle velocities arise because of the irregular insertion of particles, turbulence in the tube of the generator, rotation of the particles themselves and collisions with the walls of the generator.

Numerical model

The numerical model that we seek to validate is FDS (ver. 6.2.0). FDS solves the basic governing conservation

Table 1. Particle velocity components (u , v , w) measured for each case using two orthogonal cameras.

Experimental cases	u (s.d.) (m s^{-1})	v (s.d.) (m s^{-1})	w (s.d.) (m s^{-1})
Re-1-non-burning	8.5 (1.49)	-0.3 (0.5)	0.8 (0.6)
Re-2-non-burning	10 (1.65)	-0.5 (0.6)	0.7 (0.6)
Re-2-burning	8.25 (1.15)	-0.3 (0.6)	0.2 (0.5)
Re-2-burning	9.55 (1.45)	-0.2 (0.6)	0.1 (0.6)

equations for mass, energy and momentum of a Newtonian fluid at low-Mach number using a second-order finite difference method. The details of the equations and solution method are provided in the technical guide (McGrattan et al. 2015b) and hence are not discussed here. FDS uses the Large-Eddy Simulation (LES) methodology with the Deardoff turbulence model to describe the gas-phase turbulence and a Lagrangian particle model to describe the solid particle transport.

FDS has an inbuilt drag model only for spherical and cylindrical shapes (McGrattan et al. 2015b); for cubiform particles whose initial, unburnt, sphericity is 0.806, it can be assumed that the spherical drag model would be sufficient. Sphericity (Wadell 1933) is the surface area of a sphere with equal volume to the particle divided by the surface area of the particle. As the particle combusts, the sphericity will change; however, over a short combustion time, the sphericity is unlikely to change significantly enough to affect the drag coefficient in a meaningful way. The effect of sphericity and tumbling of a particle will tend to average out on the 20-cm wide distribution grid, which was already observed for non-burning cubiform firebrands (Wadhvani et al. 2017b). This aspect is a crucial assumption for short-range spotting, such as occurs inside a forest canopy, where particles have short flight times as compared with long-range spotting and the focus of the present study. Moreover, it is important to explore replacing the existing drag model in FDS with a generic drag model that could be used to represent a generic shape of firebrand that is neither spherical nor cylindrical. Thus, four drag models found in the literature were selected that are widely used and applicable to a generic shape of particle based on its sphericity; for this reason, no direct comparisons of drag coefficient were attempted. These models are the Haider and Levenspiel (1989), Ganser (1993), Hölzer and Sommerfeld (2008), and Bagheri and Bonadonna (2016) drag models; details can be found in Table 2.

Fig. 2 shows a representation of the different drag models used in the present study for cubiform particles, with two vertical lines representing the approximate variation of the Reynolds number during the flight time of the firebrand particles. The Reynolds number (Re_p) used is based on the particle length scales:

$$Re_p = \frac{\rho_{\text{air}} L_{\text{particle}}}{\mu_{\text{air}}(T)} |V_{\text{particle}} - V_{\text{flow}}|$$

where the $v_{\text{subscript}}$ refers to the velocity of the particle or flow, ρ is the density, μ the (temperature-dependent) viscosity and L is the particle length (McGrattan et al. 2015b).

The variation occurred owing to dissipation of the flow velocity from the mouth to downstream. Near the ground, the Reynolds number is approximately 3×10^3 and near the mouth of the generator, at the higher flow velocity, the Re is approximately 3.4×10^5 . The difference between FDS inbuilt and drag models found in the literature is due to

Table 2. List of drag models tested in this work. See references provided for definitions and explanations of equations.

Serial no.	Drag model	Drag correlation	Eqn. No.
1	FDS Spherical drag model (McGrattan <i>et al.</i> 2015b)	$C_{D, sph} = \begin{cases} \frac{24}{Re_D}, & Re_D < 1 \\ \frac{24(0.85 + 0.15 Re_D^{0.687})}{Re_D}, & 1 < Re_D < 1000 \\ 1, & Re_D > 1000 \end{cases}$	(3)
2	Haider & Levenspiel drag model (Haider and Levenspiel 1989)	$C_{D, Ha} = \frac{24}{Re_D} (1 + A Re_D^B) + \frac{C}{1 + \frac{D}{Re_D}}, \quad Re_D < 2.6 \times 10^5$ <p>where</p> $A = \exp(2.3288 - 6.4581\psi + 2.4486\psi^2)$ $B = 0.0964 + 0.5565\psi$ $C = \exp(4.905 - 13.8944\psi + 18.4222\psi^2 - 10.2599\psi^3)$ $D = \exp(1.4681 + 12.2584\psi - 20.7322\psi^2 + 15.8855\psi^3)$ <p>ψ = Sphericity of the particle</p>	(4)
3	Ganser drag model (Ganser 1993)	$\frac{C_{D, Ga}}{K_2} = \frac{24}{Re_D K_1 K_2} (1 + 0.1118(Re_D K_1 K_2)^{0.6567}) + \frac{0.4305}{1 + \frac{3305}{Re_D K_1 K_2}}, \quad Re_D K_1 K_2 \leq 10^5$ <p>where</p> <p>K_1 & K_2 is shape factor in Stokes and Newton regimes</p> <p>For isometric particle, $K_1 = [0.3333 + 0.6667\psi^{-0.5}]^{-1}$ and $K_2 = 10^{1.8148(-\log \psi)^{0.5743}}$</p>	(5)
4	Hölzer & Sommerfeld drag model (Hölzer and Sommerfeld 2008)	$C_{D, Ho} = \frac{8}{Re_D \sqrt{\psi_{\perp}}} + \frac{16}{Re_D \sqrt{\psi}} + \frac{3}{\sqrt{Re_D} \psi^{0.75}} + 0.42 \cdot 10^{0.4(-\log \psi)^{0.2}} \frac{1}{\psi_{\perp}}, \quad Re_D \leq 10^7$ <p>where</p> <p>ψ_{\perp} is called as a crosswise sphericity</p>	(6)
5	Bagheri & Bonadonna drag model (Bagheri and Bonadonna 2016)	$C_{D, Ba} = \frac{24k_S}{Re_D} \left(1 + 0.125 \left(Re_D \frac{k_N}{k_S} \right)^{\frac{2}{3}} \right) + \frac{0.46k_S}{1 + \frac{5330}{Re_D \frac{k_N}{k_S}}}, \quad Re_D < 3 \times 10^5$ <p>where</p> $k_S = \frac{\left(\frac{1}{F_S^3} + F_S^{-1} \right)}{2}, \quad k_N = 10^{\alpha_2 [-\log(F_N)] \beta_2},$ $\alpha_2 = 0.45 + \frac{10}{\exp(2.5 \log(\rho') + 30)}, \quad \beta_2 = 1 - \frac{37}{\exp(3 \log(\rho') + 100)}$ <p>apparent density (ρ') = $\frac{\rho_{solid, particle}}{\rho_{fluid, air}}$, $F_S = fe^{1.3} \frac{d_{eq}^3}{LIS}$</p> <p>$F_N = f^2 e^{\frac{d_{eq}^3}{LIS}}$, flatness of article ($f$) = S/l, elongation of particle (e) = l/L, and d_{eq} = equivalent diameter of particle</p>	(7)

simplification of the drag law adopted for spherical particles in FDS. Hölzer and Sommerfeld (2008) measured the difference between experimental and predicted drag coefficients of different drag models for different shapes. They observed that for cuboidal- and cylindrical-shaped particles, using Haider and Levenspiel, Ganser and their own drag model showed mean relative deviations in estimating drag coefficient of 42.3, 38.4 and 29% respectively. Furthermore, they observed the maximum to minimum relative deviation in estimating drag coefficients varied by three orders of

magnitude. Thus, inherently, the drag models found in the literature already have significant differences, yet have been accepted for major engineering applications.

The combustion of firebrands is represented using the inbuilt FDS single-step model considering a single fuel species that is composed primarily of C, H, O and N reacting with oxygen in one mixing-controlled step to form H₂O, CO₂, soot and CO. The details of the combustion model can be found in the FDS technical guide (McGrattan *et al.* 2015b).

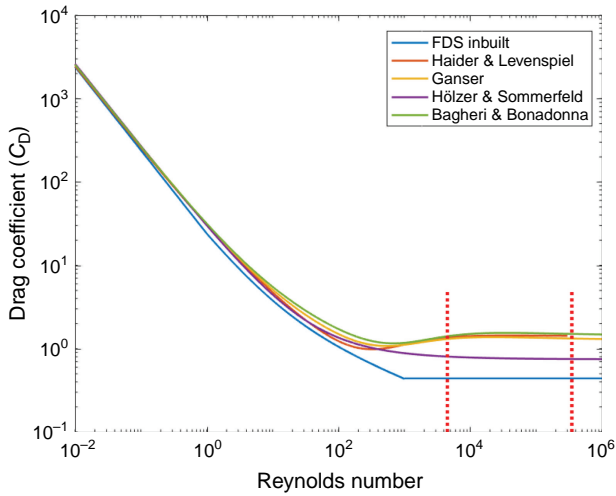


Fig. 2. Variation of different drag models (listed in Table 2) in estimating drag coefficient with Reynolds numbers (corresponding to V_{centre} 23.4 and 25.9 m s^{-1}) considered in the present study for cubiform firebrands. The two dotted red lines show the variation of Reynolds number during the flight time of the firebrands.

Results

The experimental measurement of flow profiles at the mouth of the generator is shown for two directions (Y-, Z-direction) orthogonal to the flow (X-direction) in Fig. 3. Uniform flow develops at the mouth of the generator for both flow cases in the orthogonal directions to the flow with a velocity at the centre (V_{centre}) of 23.4 and 25.9 m s^{-1} respectively. After developing a uniform flow field, firebrand particles are injected into the stream non-burning or burning. The extremely low feed rate ensures no particle–particle collisions and few collisions with the wall of the pipe (0–2% in each experimental run). The particle velocity components measured using a high-speed camera are detailed in Table 1. Experimental observations of firebrand distribution were compared with simulations. The simulation domain encompasses the experimental apparatus from the mouth of the generator to the distribution grid, similarly to the work with the prototype generator (Wadhvani et al. 2017b). The simulated distribution grid has the same dimensions as the experimental distribution grid. The simulation domain is 10.2 m long, 2.4 m wide and 2 m high respectively in the X, Y, and Z directions. The domain is subdivided into four parts longitudinally, $0 \leq x \leq 0.5$, $0.5 \leq x \leq 2.5$, $2.5 \leq x \leq 4.5$, and $4.5 \leq x \leq 10.2$ with uniform grid sizes ($\Delta x = \Delta y = \Delta z$) 20, 40, 40 and 40 mm respectively. The mouth of firebrand generator is placed at $x = 0$. The centre of the generator mouth is placed 1.1 m above the ground. The simulation inlet conditions were defined using the time-averaged mean flow profile measured at the firebrand generator mouth. The results were shown to be independent of the choice of grid at a flow Reynolds number of 4×10^5 , as discussed in

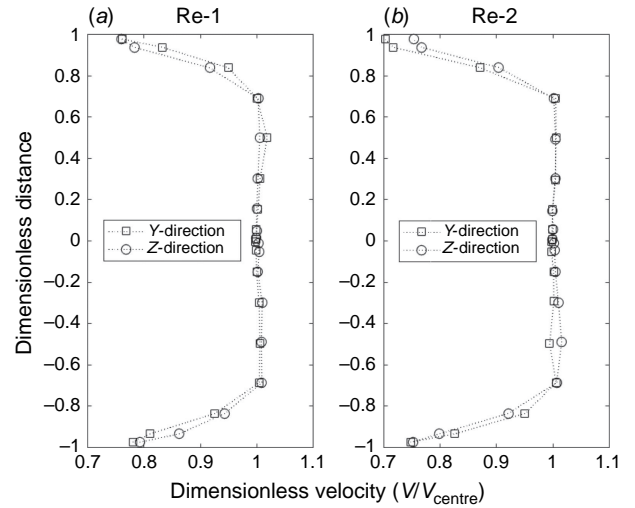


Fig. 3. Flow profile measured at the mouth of the generator using a pitot tube.

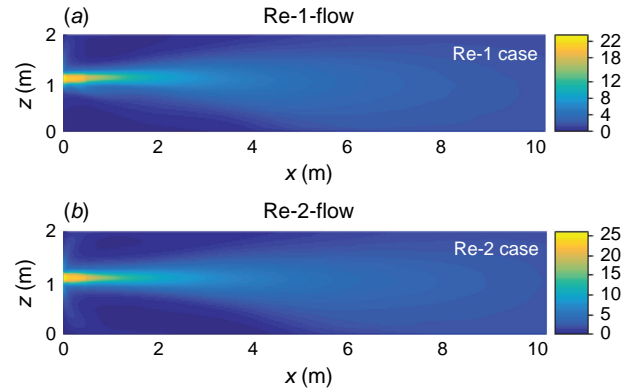


Fig. 4. Simulated mean speed contours of the generator for two flow speeds. Note that the jet for the Re-1 flow is more diffuse than for the Re-2 flow. For the Re-1 flow, the jet starts to decay significantly at ~ 2.5 m, whereas for the Re-2 flow, the jet starts to decay significantly at ~ 3.5 m.

Wadhvani (2019). Fig. 4 shows the simulated mean distribution (as contours) of the flow speed of the experimental set-up for both cases at the centre of the mouth. The presence of a strong jet flow is visible 3.5–4 m from the mouth.

After flow establishment, firebrand particles are injected into the simulation with a distribution of initial particle velocities given in Table 1.

A combination of 27 firebrand particles were injected into the domain to comprehensively represent experimental conditions with an initial component velocity equal to $u \pm \sigma_u$, $v \pm \sigma_v$, and $w \pm \sigma_w$ (representing mean and standard deviation of particle component velocities given in Table 1). Following the same methodology as Wadhvani et al. (2017b) for non-burning cubiform particles using a prototype firebrand generator, six types of Lagrangian particles are injected to represent the particle distribution density.

The six types of Lagrangian particles are defined by $\mu \pm \sigma/4$, $\mu \pm 3\sigma/4$, and $\mu \pm 3\sigma/2$; μ , σ are the mean density and standard deviation of particle densities respectively of cubiform particles = 428 kg m^{-3} . In the experiments, particles do collide with the duct. However, the simulation is initialised with particles at the mouth of the generator with some specified velocities. Therefore, particle collisions with the duct are not explicitly computed, but their cumulative effect is somewhat captured in the initial velocities of the particles.

Comparative contours between experimental and simulated firebrand distributions are plotted in Figs 5–8 for simulations using various drag models. The supplementary file provides further insight into the distribution of particles. In Figs 5–8, the solid lines are the experimental distribution. The dotted lines denote the equivalent simulated distribution; the simulated distribution meets the same convergence criteria as the experimental distribution.

For non-burning cubiform firebrands in Figs 5, 6, the simulated results overlap quite well in both the Re-1 and Re-2 cases with all drag models. The difference between the locations of the two peaks, i.e. experimental and simulated (computed using Eqn 8), was found to be less than 5% for non-burning cubiform firebrands with the following drag models:

- Re-1: FDS default, Haider and Levenspiel, Ganser and Bagheri and Bonadonna
- Re-2: FDS default, Haider and Levenspiel and Bagheri and Bonadonna

The quantitative difference found between the two peaks for each case is presented in their respective figures for all the drag models. The difference between the two peaks is computed as the ratio of the relative difference between the two peak locations from the mouth of the firebrand generator to the location of experimental peak, as represented in Eqn 8.

$$\text{difference}_{\text{peak to peak}} = \frac{\text{peak}_{\text{expt}} - \text{peak}_{\text{sim}}}{\text{peak}_{\text{expt}}}, \quad (8)$$

For burning cubiform firebrands in Figs 7, 8, the peak difference is less than 5% with the following drag models:

- Re-1: Haider and Levenspiel and Ganser
- Re-2: Haider and Levenspiel, Ganser, Bagheri and Bonadonna and Hölzer and Sommerfeld

In Figs 5–8, Haider and Levenspiel is the only drag model that resulted in less than a 5% difference in peak location for all four configurations.

In all the simulations (shown in Figs 5–8), the lateral spread of the simulated firebrand particle overlaps well with the experimental observations. The difference in lateral spread of firebrands was found to be small, i.e. 0–0.1 m or 0–7% of experimental width on either side of the peak of distribution using the Haider and Levenspiel model in all the

simulations. For other drag models (including the FDS default), inconsistent differences were observed in lateral spread, with differences varying by 0–0.5 m or 0–35% of the experimental width on either side of the peak of distribution. The lateral spread is caused in part by the initial v - and w -components of the particle velocity, which could be due to turbulence inside the firebrand generator. The lateral spread is also likely exacerbated by the rotation of the particles, which results in imbalanced drag forces and exaggerated (compared with a point particle) lateral movement. van Wachem *et al.* (2015) and Carranza and Zhang (2017) also observed a similar phenomenon when studying the transport of non-spherical particles in a confined domain. The present work considers only the point particle assumption used in FDS, which considers only the drag force acting on the particle and limits the inclusion of other forces acting on it.

The maximum distance of firebrand travel is different for each simulation. Fig. 9 shows the comparison of the peak of the firebrand distribution and maximum distance of firebrand spotting for cubiform particles using the different drag models. The whiskers in the plot represent the maximum and minimum possible spotting distances for all the cases. The comparison between the non-burning and burning cubiform firebrands for both Re cases shows that combustion of the firebrands significantly reduced the peak locations of the experimental and simulated firebrand distributions. The changes occur because of the significant reduction in particle mass and the slight reduction in particle size due to burning, which reduce the momentum of the firebrand when released from the mouth of the firebrand generator. However, a few are able to travel further from the mouth of the firebrand generator, as observed in the experiments, which may be due to collision with the surface of the pipe. The burning firebrand particles are simulated as burnable fuel and could lose mass. However, because of the short flight time (~ 1 – 2 s), the mass loss of the particles over the simulated trajectory is negligible. The vegetation pyrolysis model of FDS has been extensively validated for litter fuels (Perez-Ramirez *et al.* 2017; Wadhvani *et al.* 2017a; Wadhvani 2019) and many other materials (Moinuddin *et al.* 2020), and so we believe the simulation should provide a good estimate of the in-flight mass loss of the experimental particles. Because the simulated mass loss is negligible over the flight time, we do not believe that mass loss has significant effect on the landing distribution in the experiments.

The Haider and Levenspiel drag model arguably gives a better comparative prediction of peak location of firebrand distribution and maximum spotting distance as compared with other drag models for burning firebrands. The Ganser model appears to be second best, because its Re-2 non-burning prediction is not as good as the Haider and Levenspiel model. Although the default drag model provides a reasonable prediction for the non-burning firebrands,

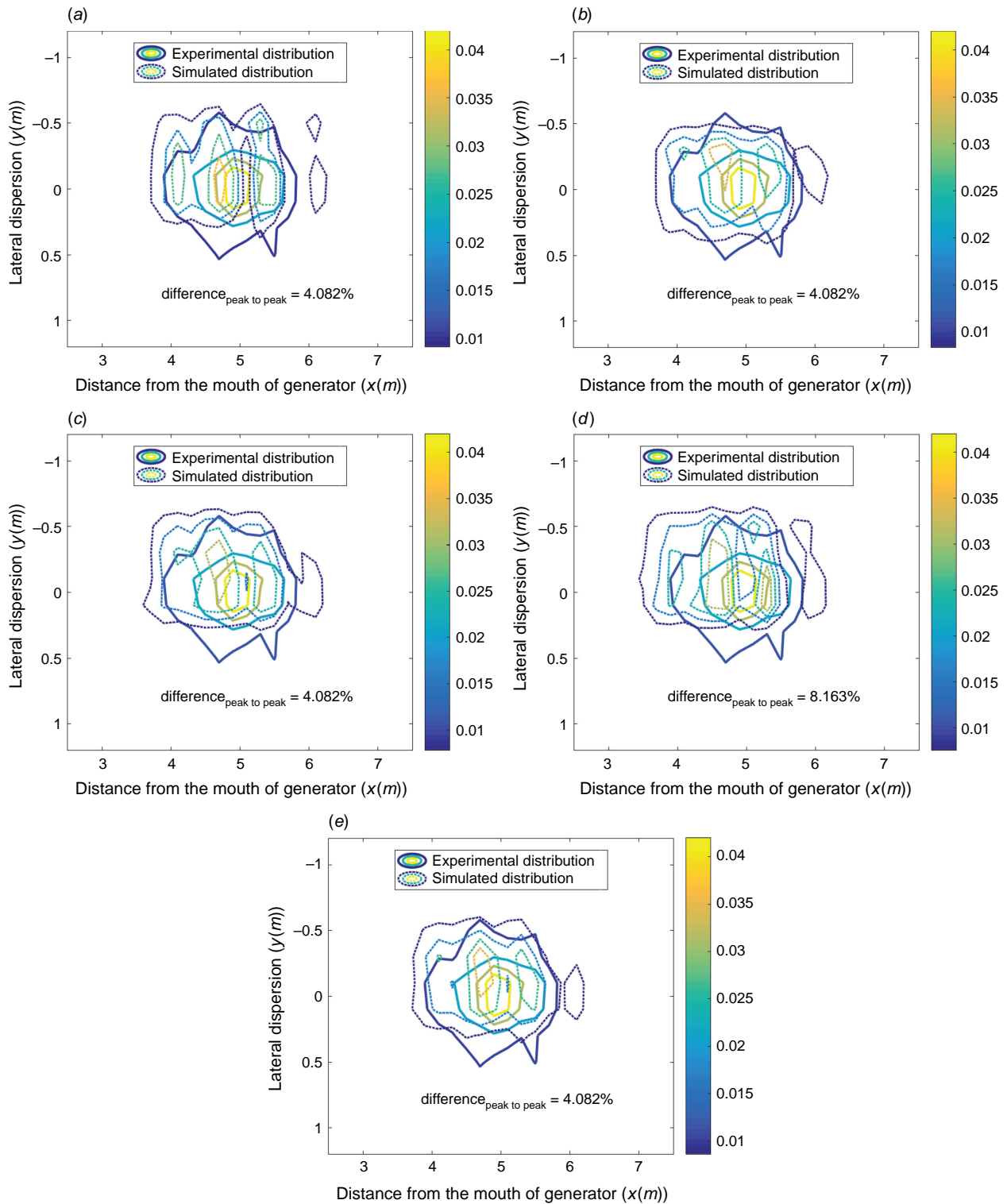


Fig. 5. Comparative contours (experimental and simulated) of firebrand distribution for non-burning cubiform particles at Re-I with all the drag models.

its prediction for burning cases is not as good. In Fig. 2, within the Re range for the present study (marked two vertical lines), the drag coefficients from Haider and Levenspiel,

Ganser and Bagheri and Bonadonna models are very close to each other, and overall, these models give better results other the two models.

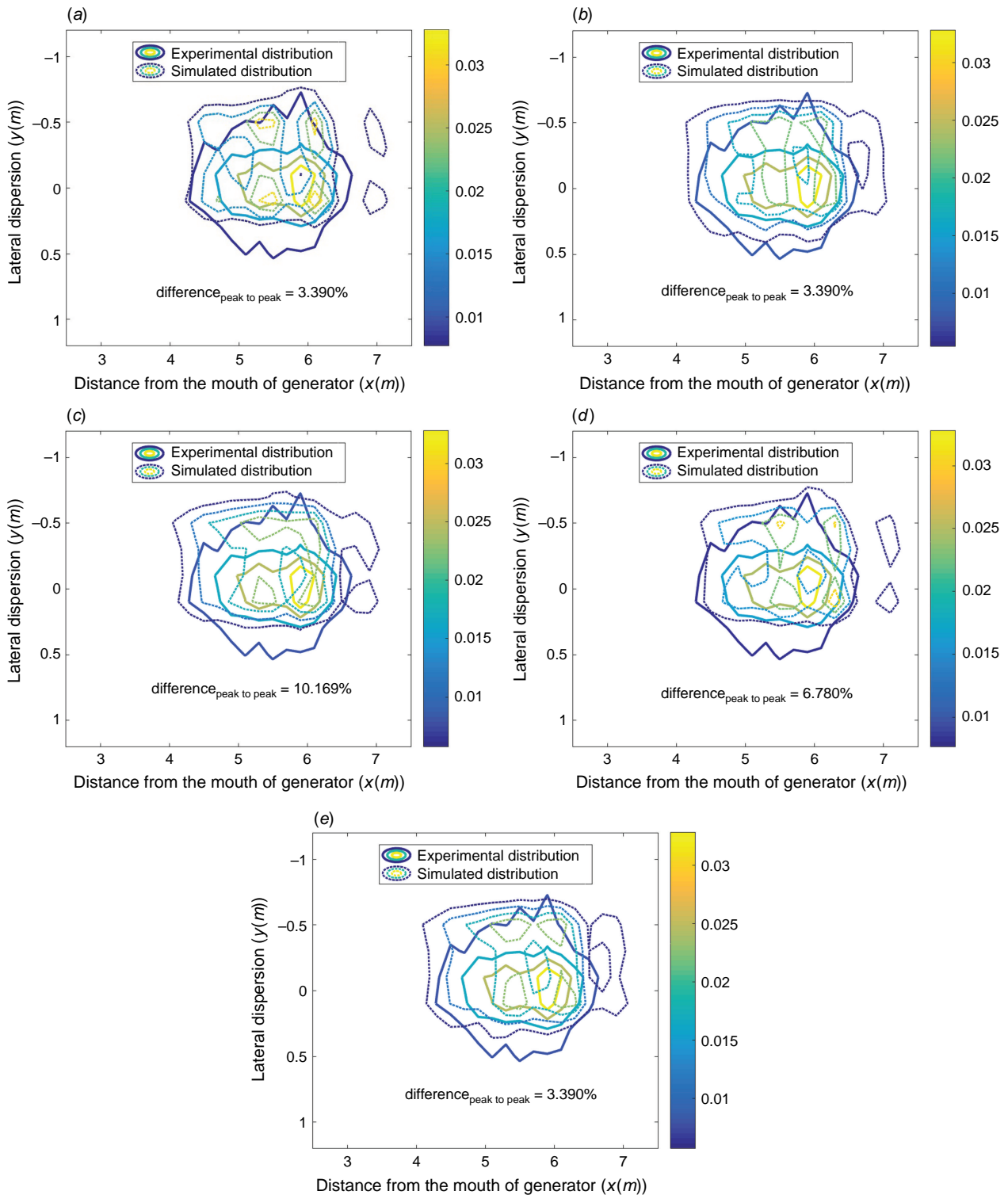


Fig. 6. Comparative contours (experimental and simulated) of firebrand distribution for non-burning cubiform particles at Re-2 with all the drag models.

When comparing the lateral distribution of firebrands predicted by the Haider and Levenspiel model (Haider and Levenspiel 1989) and the Ganser model (Ganser 1993), it can be seen that the Haider and Levenspiel model shows a

consistent overlaps with the experimental spread. This aspect (comparing lateral distribution) becomes profound when other shapes, such as cylindrical and square disc-shaped firebrand particles, are considered, as observed by Wadhvani (2019)

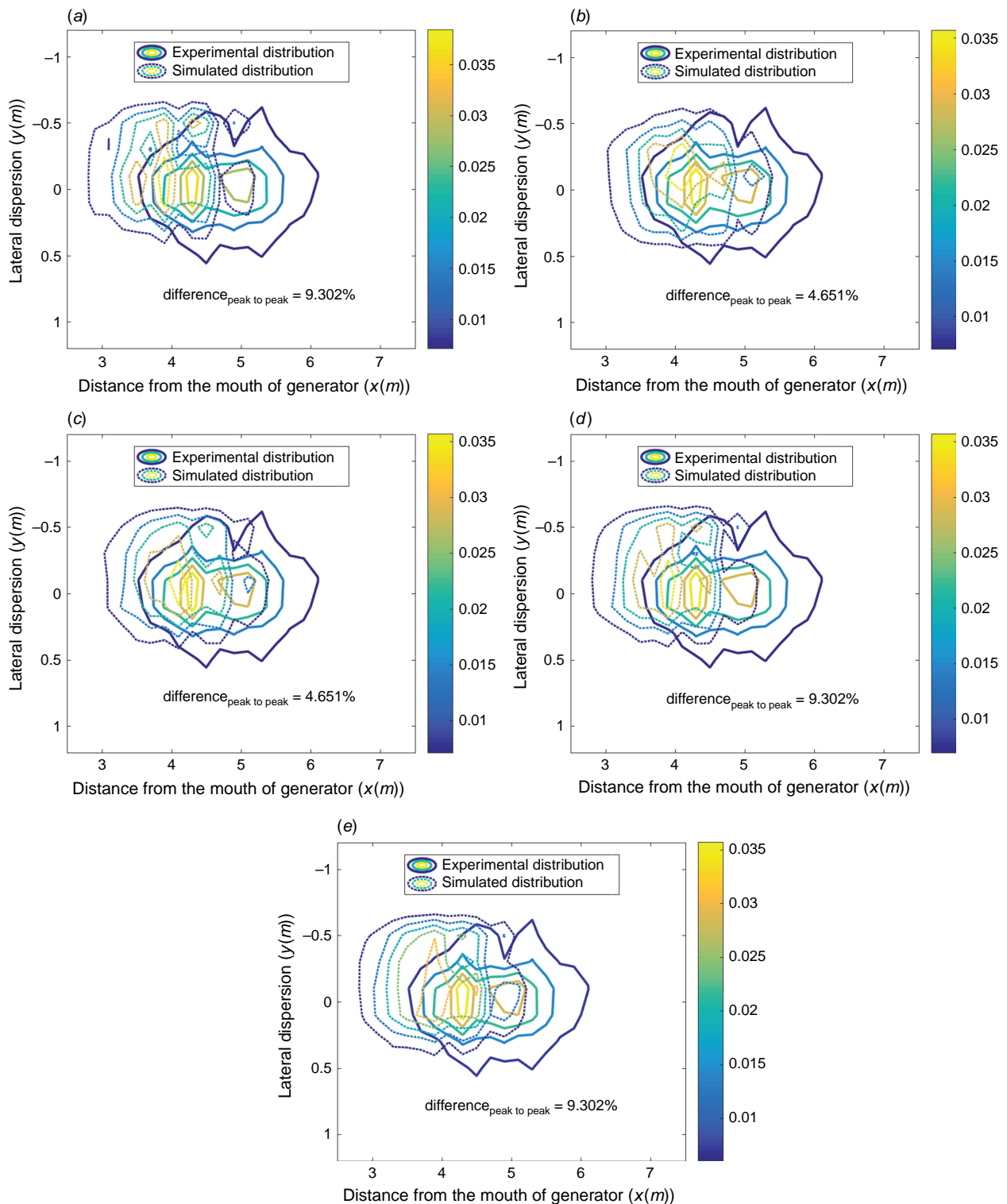


Fig. 7. Comparative contours (experimental and simulated) of firebrand distribution for burning cubiform particles at Re-I with all the drag models.

and Wadhvani et al. (2021) for non-burning particles. A similar comparison can be drawn for the maximum and minimum spotting distances by comparing the whiskers in Fig. 9.

In this case, all of the particle distributions are two-dimensional and there are no well-established statistical tests, without significant limitations, to rigorously compare

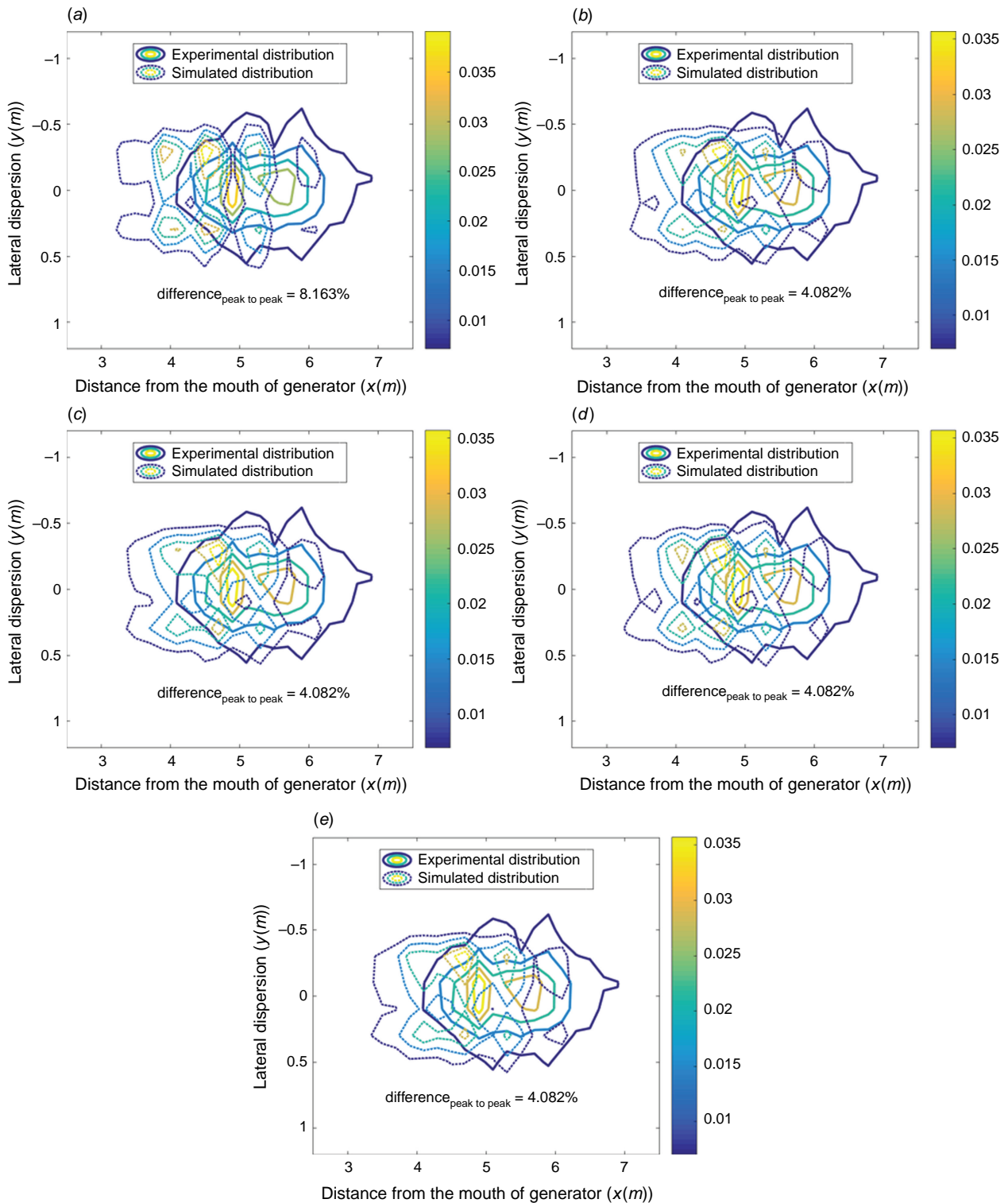


Fig. 8. Comparative contours (experimental and simulated) of firebrand distribution for burning cubiform particles at Re-2 with all the drag models.

bivariate distributions. A bivariate Kolmogorov–Smirnov test has been described in the literature; however, there is no rigorous way to order bivariate data. A discussion of the limitations

for tests for bivariate distributions may be found in [Quill et al. \(2020\)](#). It may be possible to develop a bespoke test for our datasets, but this is beyond the scope of the present work.

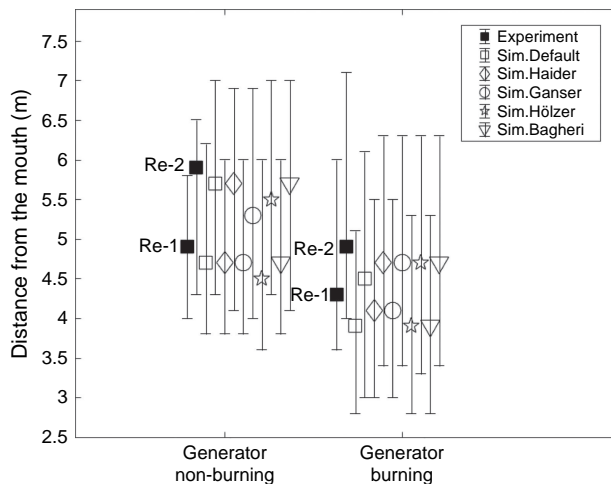


Fig. 9. Comparison between the observed experimental and simulated peaks of firebrand distribution using a full-scale generator with the different drag models. The whiskers represent the maximum and minimum distances of particle transport.

Conclusion

The movement of firebrand particles in a wildfire can be simulated using a Lagrangian model because the particles are too small to significantly alter the driving and pyrogenic winds. We constructed a novel firebrand generator that produces a uniform flow with a series of non-burning and burning firebrands with varied firebrand shapes and sizes, flow speeds and combustion stages. The firebrand generator was used to conduct a benchmark experiment that is used to validate a Lagrangian submodel of Fire Dynamics Simulator (FDS) for cubiform firebrands, both non-burning and burning, at two flow speeds.

The simulated results using FDS were found to closely represent the experimental observations for the distribution of the first-impact location of firebrands. The uncertainties in the measurements and simulations are quantified throughout the manuscript. The experimental distributions are allowed to converge until a maximum 5% variation, the uncertainties in the simulated distributions are quantified by the minimum and maximum statistics provided in Fig. 9; mean deviations in estimates of drag coefficients are provided as appropriate, and the difference between the peaks of the experimental and simulated distributions is quantified. The simulation was found to practically predict the lateral spread of firebrands with negligible differences, 0–0.1 m (i.e. 0–7% of experimental width) on either side of the peak of distribution using the Haider and Levenspiel drag model. This difference in lateral spread is significantly higher and inconsistent in the other drag models. However, the peak location of firebrand distribution using the Haider and Levenspiel drag model was found to be slightly underpredicted (< 5%) compared with the experimental peak location of distribution. The underprediction could be due to an inherent error in estimating drag coefficients by the drag model (Hölzer and Sommerfeld 2008). The maximum

spotting distances with the non-burning firebrands were found to be in good agreement with the experimental observations, with an overprediction of 8–12% from the experimental values. For the burning firebrands, the simulated maximum spotting distance of cubiform firebrands was underpredicted by 15–20% compared with the experimental values. The most likely reason for this is simplified representation of the experiments while conducting simulations. In the experiments, there is a possibility that there were a greater number of firebrands heavier than the average firebrand. Only a fraction of the firebrands (30 out of 250) was used to estimate the properties of the firebrands required for simulation.

The Haider and Levenspiel drag model, as compared with the other drag models considered, was found to be better suited for firebrands to estimate the firebrand distribution and this could be used as an alternative drag model to study transport of firebrands with FDS. The FDS inbuilt drag models are restricted to only two shapes of firebrand particle, i.e. spherical and cylindrical. The Haider and Levenspiel drag model presents an alternative choice as a generic shape factor-based drag model. However, further study, similar to the one here, is required for different firebrand characteristics (e.g. size, shape, combustion phase) and flow speeds to fully quantify the error associated in estimating spotting distance. Our novel firebrand generator can be used to conduct such validation studies of Lagrangian submodels with different shapes, rates of combustion and Reynolds numbers in future studies. Some preliminary comparisons of different shapes appear in Wadhvani et al. (2021).

The models tested in this study were developed empirically, by curve fitting to the results of free-fall (rather than forced-flow) tests. All the models attempt to account for irregularly shaped particles by incorporating some estimates of sphericity of the particles. The Haider and Levenspiel model uses only the classical definition of sphericity, whereas Ganser introduces shape factors, Hölzer and Sommerfeld use an additional measure of cross-wise sphericity, and Bagheri and Bonadonna use an elongation and equivalent diameter of the particle. Because these models are essentially complicated functions that fit the observed, it is difficult to appraise the features of each model in a different context based on the landing distribution data that we measured. Our results imply that the more complicated estimates of shape are not necessarily appropriate for estimating drag coefficients in our flows.

Extending the modelling to complete fire conditions is challenging. After modelling transport for general firebrand shapes, the most important factor is modelling the combustion of firebrands along the flight path. The rate of combustion along the flight path would be particularly difficult to estimate, and the atmospheric conditions, such as a possibly reduced level of oxygen, would likely influence the combustion rate.

Supplementary information

Supplementary material is available [online](#).

References

- Albini, FA (1979) Spot fire distance from burning trees- a predictive model. General Technical Report INT-GTR-56. Ogden, UT: USDA Forest Service, Intermountain Forest and Range Experiment Station. 73 p.
- Bagheri G, Bonadonna C (2016) On the drag of freely falling non-spherical particles. *Powder Technology* **301**, 526–544. doi:10.1016/j.powtec.2016.06.015
- Carranza F, Zhang Y (2017) Study of drag and orientation of regular particles using stereo vision, Schlieren photography and digital image processing *Powder Technology* **311**, 185–199. doi:10.1016/j.powtec.2017.01.010
- Cruz, MG, Gould, JS, Alexander, ME, Sullivan, AL, McCaw, WL, Mathews, S (2015) 'Guide to rate of fire spread models for Australian vegetation.' (CSIRO Land and Water Flagship: Canberra, ACT and AFAC: Melbourne, Vic.)
- El Houssami M, Mueller E, Filkov A, Thomas JC, Skowronski N, Gallagher MR, Clark K, Kremens R, Simeoni A (2016) Experimental procedures characterising firebrand generation in wildland fires. *Fire Technology* **52**, 731–751. doi:10.1007/s10694-015-0492-z
- Filkov A, Prohanov S, Mueller E, Kasymov D, Martynov P, El Houssami M, Thomas J, Skowronski N, Butler B, Gallagher M (2017) Investigation of firebrand production during prescribed fires conducted in a pine forest. *Proceedings of the Combustion Institute* **36**, 3263–3270. doi:10.1016/j.proci.2016.06.125
- Ganser GH (1993) A rational approach to drag prediction of spherical and nonspherical particles. *Powder Technology* **77**, 143–152. doi:10.1016/0032-5910(93)80051-B
- Gould JS, McCaw W, Cheney N, Ellis P, Knight I, Sullivan A (2008) 'Project Vesta: fire in dry eucalypt forest: fuel structure, fuel dynamics and fire behaviour.' (CSIRO Publishing)
- Haider A, Levenspiel O (1989) Drag coefficient and terminal velocity of spherical and non-spherical particles. *Powder Technology* **58**, 63–70. doi:10.1016/0032-5910(89)80008-7
- Hölzer A, Sommerfeld M (2008) New simple correlation formula for the drag coefficient of non-spherical particles. *Powder Technology* **184**, 361–365. doi:10.1016/j.powtec.2007.08.021
- Kortas S, Mindykowski P, Consalvi JL, Mhiri H, Porterie B (2009) Experimental validation of a numerical model for the transport of firebrands. *Fire Safety Journal* **44**, 1095–1102. doi:10.1016/j.firesaf.2009.08.001
- Lain S, Garcia JA (2006) Study of four-way coupling on turbulent particle-laden jet flows *Chemical Engineering Science* **61**(20), 6775–6785. doi:10.1016/j.ces.2006.07.005
- Linteris, GT, Gewuerz, L, McGrattan, KB, Forney, GP (2004) Modeling solid sample burning with FDS. NIST Interagency/Internal Report (NISTIR), National Institute of Standards and Technology, Gaithersburg, MD. doi:10.6028/NIST.IR.7178.
- Manzello SL, Suzuki S (2013) Experimentally simulating wind driven firebrand showers in Wildland-Urban Interface (WUI) fires: overview of the NIST firebrand generator (NIST Dragon) technology. *Procedia Engineering* **62**, 91–102. doi:10.1016/j.proeng.2013.08.047
- Manzello SL, Suzuki S (2014) Exposing decking assemblies to continuous wind-driven firebrand showers. *Fire Safety Science* **11**, 1339–1352. doi:10.3801/IAFSS.FSS.11-1339
- Manzello SL, Cleary TG, Shields JR, Yang JC (2006) Ignition of mulch and grasses by firebrands in wildland-urban interface fires. *International Journal of Wildland Fire* **15**, 427–431. doi:10.1071/WF06031
- Manzello SL, Shields JR, Cleary TG, Maranghides A, Mell WE, Yang JC, Hayashi Y, Nii D, Kurita T (2008) On the development and characterisation of a firebrand generator. *Fire Safety Journal* **43**, 258–268. doi:10.1016/j.firesaf.2007.10.001
- McArthur AG (1967) 'Fire behaviour in eucalypt forests.' (Commonwealth of Australia, Department of National Development: Canberra, ACT, Australia)
- McGrattan K, McDermott R, Weinschenk C, Overholt K, Hostikka S, Floyd J (2015a) 'Fire dynamics simulator user's guide', 6th edn. (National Institute of Standards and Technology: Gaithersburg, Maryland, USA)
- McGrattan K, McDermott R, Weinschenk C, Overholt K, Hostikka S, Floyd J (2015b) 'Fire Dynamics Simulator Technical Reference Guide Volume 1: Mathematical Model.' (National Institute of Standards and Technology: Gaithersburg, Maryland, USA)
- Moinuddin K, Razzaque QS, Thomas A (2020) Numerical simulation of coupled pyrolysis and combustion reactions with directly measured fire properties. *Polymers* **12**, 2075. doi:10.3390/polym12092075
- Perez-Ramirez Y, Mell WE, Santoni P-A, Tramon J-B, Bosseur F (2017) Examination of WFDS in modeling spreading fires in a furniture calorimeter. *Fire Technology* **53**, 1795–1832. doi:10.1007/s10694-017-0657-z
- Quill R, Sharples JJ, Sidhu LA (2020) A statistical approach to understanding canopy winds over complex terrain *Environmental Modeling & Assessment* **25**(2), 231–250. doi:10.1007/s10666-019-09674-w
- Sardoy N, Consalvi JL, Kaiss A, Fernandez-Pello AC, Porterie B (2008) Numerical study of ground-level distribution of firebrands generated by line fires. *Combustion and Flame* **154**, 478–488. doi:10.1016/j.combustflame.2008.05.006
- Storey MA, Price OF, Bradstock RA, Sharples JJ (2020) Analysis of variation in distance, number, and distribution of spotting in south-east Australian wildfires. *Fire* **3**, 10. doi:10.3390/fire3020010
- Suzuki S, Johnsson E, Maranghides A, Manzello SL (2016) Ignition of wood fencing assemblies exposed to continuous wind-driven firebrand showers. *Fire Technology* **52**, 1051–1067. doi:10.1007/s10694-015-0520-z
- Tarifa CS (1967) Transport and combustion of firebrands. Final report of Grants FG-SP-114 and FG-SP-146, Vol. 2. Instituto Nacional de Tecnica Aeroespacial, Esteban Terradas. (Madrid, Spain).
- Tarifa CS, del Notario PP, Moreno FG (1965) On the flight paths and lifetimes of burning particles of wood. In 'Proceeding of Combustion Institute'. Vol. 10, pp. 1021–1037.
- Thomas JC, Mueller EV, Santamaria S, Gallagher M, El Houssami M, Filkov A, Clark K, Skowronski N, Hadden RM, Mell W, Simeoni A (2017) Investigation of firebrand generation from an experimental fire: development of a reliable data collection methodology. *Fire Safety Journal* **91**, 864–871. doi:10.1016/j.firesaf.2017.04.002
- Thomas CM, Sharples JJ, Evans JP (2020) The terminal-velocity assumption in simulations of long-range ember transport. *Mathematics and Computers in Simulation* **175**, 96–107. doi:10.1016/j.matcom.2019.08.008
- Thurston W, Kepert JD, Tory KJ, Fawcett RJB (2017) The contribution of turbulent plume dynamics to long-range spotting *International Journal of Wildland Fire* **26**(4), 317. doi:10.1071/wf16142
- Tohidi A, Kaye NB (2017) Comprehensive wind tunnel experiments of lofting and downwind transport of non-combusting rod-like model firebrands during firebrand shower scenarios *Fire Safety Journal* **90**, 95–111. doi:10.1016/j.firesaf.2017.04.032
- Tse SD, Fernandez-Pello AC (1998) On the flight paths of metal particles and embers generated by power lines in high winds – a potential source of wildland fires. *Fire Safety Journal* **30**, 333–356. doi:10.1016/S0379-7112(97)00050-7
- van Wachem B, Zastawny M, Zhao F, Mallouppas G (2015) Modelling of gas-solid turbulent channel flow with non-spherical particles with large Stokes numbers *International Journal of Multiphase Flow* **68**, 80–92. doi:10.1016/j.ijmultiphaseflow.2014.10.006
- Wadell H (1933) Sphericity and Roundness of Rock Particles *The Journal of Geology* **41**(3), 310–331. doi:10.1086/624040
- Wadhvani R (2019) Physics-based simulation of short-range spotting in wildfires. PhD thesis. Victoria University, Melbourne, Australia.
- Wadhvani R, Sutherland D, Moinuddin K (2017a) Suitable pyrolysis model for physics-based bushfire simulation. In '11th Asia-Pacific Conference on Combustion'. University of Sydney, Sydney', 10–14 December 2017. (eds Masri AR, Cleary M, Dunn M, Kourmatzis A, Hawkes ER, Kook S and Chan QN) pp. 582–585. ISBN: 978-1-5108-5646-2.
- Wadhvani R, Sutherland D, Ooi A, Moinuddin K, Thorpe G (2017b) Verification of a Lagrangian particle model for short-range firebrand transport. *Fire Safety Journal* **91**, 776–783. doi:10.1016/j.firesaf.2017.03.019
- Wadhvani R, Sutherland D, Moinuddin K (2019) Simulated transport of short-range embers in an idealised bushfire, In 'Proceeding for the 6th International Fire Behavior and Fuels Conference'. Sydney, Australia, April 29–May 3, 2019.
- Wadhvani R, Sutherland D, Thorpe G, Moinuddin K (2021) Improvement of drag model for non-burning firebrand transport in Fire Dynamics Simulator. In 'MODSIM2021, 24th International Congress on Modelling and Simulation', December 2021. (Eds Vervoort RW, Voinov, AA, Evans, JP and Marshall, L) pp. 85–91. (Modelling and Simulation Society of Australia and New Zealand) ISBN: 978-0-9872143-8-6.

Data availability. The data used to generate the results in the paper will be made available on reasonable request.

Conflicts of interest. There is no conflict of interest.

Declaration of funding. The financial support for this study was provided by Bushfire and Natural Hazards CRC, Australia.

Acknowledgements. The authors would like to acknowledge the technical support provided by Mr Lyndon Macindoe and Mr Philip Dunn during the experimental study. We also acknowledge computational support provided by the Spartan HPC team of the University of Melbourne.

Author affiliations

^ACentre for Environmental Safety and Risk Engineering, Victoria University, Melbourne, Vic. 3030, Australia.

^BBushfire and Natural Hazards Cooperative Research Centre (CRC), Melbourne, Vic. 3002, Australia.

^CSchool of Science, University of New South Wales, Canberra, ACT 2600, Australia.

^DDepartment of Mechanical Engineering, University of Melbourne, Vic. 3052, Australia.